Combustion and Flame 162 (2015) 4102–4111

Contents lists available at ScienceDirect

Combustion and Flame

journal homepage: www.elsevier.com/locate/combustflame

End-gas autoignition and detonation development in a closed chamber

Hao Yu, Zheng Chen*

SKLTCS, Department of Mechanics and Engineering Science, College of Engineering, Peking University, Beijing 100871, China

ARTICLE INFO

Article history:
Received 9 March 2015
Revised 24 August 2015
Accepted 25 August 2015
Available online 16 September 2015

Keywords:
Autoignition
Pressure wave
Detonation
End-gas
Hydrogen/air

ABSTRACT

It is generally accepted that knock in spark ignition engines might be caused by end-gas autoignition. However, the detailed mechanism for autoignition-induced pressure oscillation and detonation development is still not well understood. This work studied end-gas autoignition and detonation development in a closed chamber using 1D simulation. Stoichiometric hydrogen/air mixture at different initial temperatures and pressures was considered and detailed chemistry was included in simulation. The objectives were to identify possible modes of end-gas combustion and to understand the mechanism of autoignition-induced pressure wave and detonation development. Depending on the chamber length as well as the initial temperature and pressure, there are three modes of end-gas combustion: normal flame propagation without autoignition, autoignition without detonation development, and detonation development. The amplitude of pressure oscillation was found to be determined by the mode of end-gas autoignition: autoignition can induce high amplitude of pressure oscillation similar to conventional knock; and detonation development can cause extremely high amplitude of pressure oscillation similar to super-knock. It was shown that autoignition and detonation development can be induced by increasing the initial temperature, initial pressure, or chamber length. The evolution of states of different flow particles was tracked and the combustion mode was found to switch from constant-pressure to constant-volume when autoignition occurs. The coupling between pressure wave and chemical reaction was analyzed and the mechanism for autoignition front acceleration and detonation development was investigated. Moreover, autoignition in end-gas with different values of ignition progress was simulated. It was demonstrated that high reactivity of end-gas promotes autoignition and detonation development.

1. Introduction

Downsized and boosted direct injection spark ignition engines (SIE) have the advantages of higher thermal efficiency and higher power density compared to traditional gasoline engine with large displacement. Therefore, it can be used to reduce fuel consumption. However, in highly-boosted gasoline engines, there is stronger tendency of knock when the premixture is compressed to higher temperature and pressure [1–4]. When knock occurs, high-frequency pressure oscillation can cause severe engine damage.

It is generally accepted that knock in spark ignition engines is caused by end-gas autoignition [5–7]. When premixed flame propagates in a closed chamber, the unburned gas (end-gas) is progressively compressed and its temperature and pressure continuously increase. Under appropriate conditions, autoignition occurs in end-gas before the propagating flame can consume the fuel. Heat release during local autoignition generates pressure pulse/wave which propagates across the system. The unburned mixture immediately behind the pressure wave might be compressed to react rapidly and, in turn, further enhance the pressure wave [4, 5, 7]. A detonation develops if there is a coherent coupling between pressure wave and local reaction/autoignition [8, 9]. The pressure wave propagates back-and-forth inside the closed chamber since it is reflected on the boundary walls. Consequently, high-frequency pressure oscillation or knock occurs.

In the literature, there are extensive studies on end-gas autoignition since it is closely related to engine knock. Theoretically, Strickland-Constable [59] and Livengood and Wu [10] studied flame propagation in an auto-ignitive mixture and proposed an integral method to predict the occurrence of autoignition; Zel'dovich [8, 11] first analyzed different modes of reaction front propagation caused by autoignition in a mixture with non-uniform reactivity; Bradley and coworkers [3, 6, 12–15] further investigated autoignition from a hot spot and proposed an operational peninsula in the plot of two non-dimensional parameters, namely the normalized temperature gradient and the ratio of acoustic time to excitation time (the operational peninsula can be used to determine the critical conditions for detonation development); Kagan and Sivashinsky [16, 17] analyzed end-gas autoignition in a one-dimensional (1D) closed chamber and proposed a 0D model to predict autoignition. However, one-step global

* Corresponding author.
E-mail address: cz@pku.edu.cn, chenzheng@coe.pku.edu.cn (Z. Chen).

http://dx.doi.org/10.1016/j.combustflame.2015.08.018
0010-2180/

reaction was usually assumed in theoretical analysis. Since complicated chemical kinetics is involved in ignition process, detailed chemistry needs to be considered for end-gas autoignition.

Experimentally, high speed photograph technology was used to visualize end-gas autoignition in engine (e.g., [2, 18, 19]) and rapid compression machine (RCM) [4, 20, 21]. Inside the engine and RCM, the flame front and flow are three-dimensional and thereby it is difficult to understand the interaction between pressure wave and chemical reaction during the autoignition process. To overcome this difficulty, Nagano et al. [22] and Qi et al. [23] designed quasi 1D experiment using a closed tube-shaped vessel to study end-gas autoignition and pressure oscillation. In these experiments, end-gas autoignition was successfully observed. However, the process is not truly 1D since there is strong flame-boundary layer interaction during flame propagation in a tube. Consequently, such experiments still have limitations in terms of understanding autoignition and pressure wave-chemistry interaction. (The truly 1D experiment for end-gas autoignition is to use a spherical bomb: first the premixture is preheated to high-enough temperature; then the mixture is centrally ignited which results in an outwardly propagating spherical flame; finally autoignition occurs in the unburned mixture after it is compressed by the outwardly propagating spherical flame. However, the spherical bomb might be damaged by strong pressure oscillation or detonation induced by end-gas autoignition.)

Numerically, multi-dimensional simulations were conducted to investigate the end-gas autoignition process. For examples, Pan et al. [24, 25] conducted 2D simulations to identify distinct autoignition modes and their contribution to knock; Liberman et al. [26, 27] conducted 2D and 3D simulations to examine the onset of autoignition; Wang et al. [28] conducted 3D simulations to study the coupling between pressure wave and chemical reaction; Wei et al. [29] conducted 2D simulations to assess the effects of pressure wave on end-gas autoignition; and Chen, Yoo and coworkers conducted 2D simulations to assess the effects of turbulence on autoignition (e.g., [30–33]). Similar to experiments, the autoignition process is very complicated in multi-dimensional simulations. Moreover, complicated chemistry involved in autoignition is difficult to be included in multi-dimensional simulations. Therefore, 1D simulations were used to study the autoignition process: Ju et al. [34] identified different flame regimes of ignition in n-heptane/air mixtures; Martz et al. [35, 36] demonstrated that the autoignition process is chemically controlled and diffusion can be neglected; Zhang [37] examined the effects of thermal stratification on autoignition within the negative-temperature coefficient (NTC) regime; Dai et al. [38] demonstrated that different autoignition modes can be initialized from a cool spot when the initial temperature is in the NTC regime; and Terashima and Koshi [39] investigated the strong pressure wave generated by end-gas autoignition. However, unlike the present study, detonation development caused by end-gas autoignition was not identified in these 1D studies except our recent work [38].

This work studied end-gas autoignition and detonation development in a closed chamber using 1D simulation with detailed chemistry. The interaction between pressure wave and chemical reaction was investigated. The objectives were to identify possible modes of end-gas combustion and to understand the mechanism of autoignition-induced pressure wave and detonation development. While multidimensional simulations describe the end-gas autoignition process similar to that occurs in practice, it is difficult to explain the detailed structure (evolution of the distributions of temperature, pressure and species concentrations) of autoignition and detonation development processes which might be complicated by turbulent flow and flame-boundary layer interaction. A 1D simulation was conducted here since detailed structure of autoignition and detonation development can be readily obtained and the pressure wave-chemistry interaction can be isolated from turbulent flow and flame-boundary layer interaction.

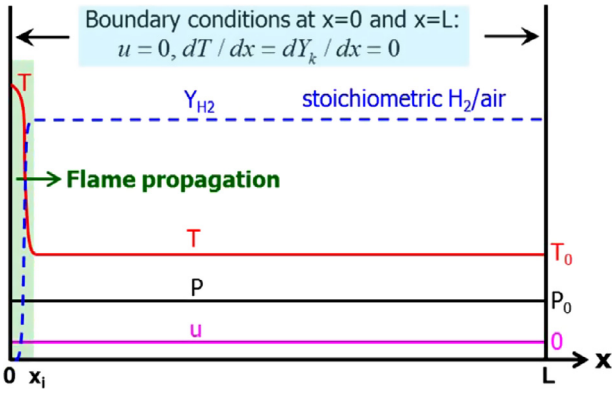

Fig. 1. The initial and boundary conditions used in the simulation of flame propagation in a 1D closed chamber with the length of L.

It should be emphasized that the in the present work we used 1D simulations to study the interaction between pressure wave and chemical reaction and the mechanism of detonation development, which are related to knock in engines. However, engine knock cannot be fully represented by simulations in the present work since our 1D simulations have the following limitations: (1) 3D effects including turbulence, boundary layer and wall heat transfer (which play major roles in engine knock) were not considered in the present 1D computation; (2) temperature inhomogeneity (local hot-spot) occurring in practical engines was not taken into account and the initial temperature of end-gas was assumed to be uniformly distributed; and (3) the fuel, initial temperature and pressure, domain dimension considered in the present study were not prototypic of an engine.

2. Model and numerical methods

2.1. Model

We conducted 1D simulation for stoichiometric hydrogen/air mixture since the chemical mechanism for hydrogen oxidation is relatively well established and it has relatively small size. In the model, the premixed H_2/air flame propagates toward the right side in a 1D closed chamber; and the end-gas between the propagating flame front and the right wall is continuously compressed and thereby autoignition and detonation might occur in the end-gas.

The computational domain is $0 \le x \le L$, where L is the chamber length. The initial and boundary conditions are presented in Fig. 1. The initial temperature and pressure of end-gas are shown to be T_0 and P_0, respectively. The propagating flame was initialized by a hot kernel close to the left boundary (i.e., $0 \le x \le x_i \approx 0.5$ mm). The initial distributions for temperature and mass fraction of all species were from PREMIX [40] results for stoichiometric H_2/air at T_0 and P_0. In PREMIX [40], finite-rate chemical kinetic model and multi-component molecular transport model were considered for a freely-propagating, adiabatic, planar flame. As shown in Fig. 1, initially the flow speed is zero (i.e., $u = 0$) everywhere and the initial pressure of P_0 is uniformly distributed in $0 \le x \le L$. The initial temperature of T_0 is uniformly distributed outside of the hot kernel (i.e., $x_i \le x \le L$). At both boundaries (i.e., $x = 0$ and $x = L$), zero flow speed and zero gradients of temperature and mass fractions are enforced.

2.2. Numerical methods

The transient flame propagation and autoignition process was simulated using the in-house code A-SURF [38, 41, 42]. The finite volume method was used in A-SURF to solve the conservation equations for 1D compressible flow with multi-components. The time evolution of the stiff reaction term was separated from that of the

Table 1
Typical cases considered for stoichiometric hydrogen/air in a 1D closed chamber.

Case	Size L	Initial T_0 and P_0	Equilibrium T_e and P_e	Observation
1	2.0 cm	900 K, 10 atm	3078 K, 30.0 atm	No autoignition, no detonation development
2	2.0 cm	1000 K, 10 atm	3110 K, 27.3 atm	Autoignition, no detonation development
3	2.0 cm	900 K, 20 atm	3130 K, 60.7 atm	Autoignition, no detonation development
4	4.0 cm	900 K, 10 atm	3078 K, 30.0 atm	Autoignition, no detonation development
5	2.0 cm	1100 K, 10 atm	3140 K, 25.2 atm	Detonation development
6	2.0 cm	1000 K, 40 atm	3217 K, 112.3 atm	Detonation development
7	20 cm	1000 K, 10 atm	3110 K, 27.3 atm	Detonation development

convection and diffusion terms by using the Strang splitting fractional-step procedure [43]. In the first and third half fractional step, the non-reactive flow was solved. The temporal integration, convective flux, and diffusive flux were calculated, respectively, using the Runge–Kutta, MUSCL-Hancock (with MINBEE flux limiter), and central difference schemes. In the second fractional step, the chemistry was solved using the VODE solver [44]. The detailed hydrogen mechanism developed by Li et al. [45] was used in simulation. CHEMKIN packages [46] were incorporated into A-SURF to calculate the thermodynamic and transport properties as well as the reaction rates. Dynamically adaptive mesh was used to accurately resolve the flame front, pressure wave, shock wave and detonation, which were always fully covered by the finest mesh with the size of 0.8 μm. The corresponding time step was $\Delta t = 10^{-10}$ s since explicit integration method was used and the Courant–Friedrichs–Lewy (CFL) number was maintained to be less than 0.5. A-SURF was successfully used in our previous studies on ignition and flame propagation (e.g., [47–50]). In our recent study [38], it was shown that A-SURF can accurately capture shock wave and detonation propagation. The details on governing equations, numerical scheme and code validation can be found in Refs. [38, 41, 42] (see the Supplementary Documents of [38, 42]) and thereby are not repeated here. Besides, the numerical resolution and grid independence were shown in the Supplementary Material of the present paper.

In simulation, the flow particles at different initial locations were tracked and their thermal states were recorded [51]. The position of a flow particle was first updated by its current flow speed (evaluated at the present time of t_n) multiplying the time step size of $\Delta t = 10^{-10}$ s; then the thermal states and flow speed of this particle at $t_n+\Delta t$ were obtained from linear extrapolation of corresponding values (evaluated at $t_n+\Delta t$) at its two neighboring grids.

3. Results and discussion

We conducted simulations for different values of chamber length L, initial temperature T_0, and initial pressure P_0. Only the results for seven typical cases were presented and discussed below. The values of (L, T_0, P_0) for these cases were summarized in Table 1, in which the equilibrium temperature T_e and pressure P_e were calculated under the conditions of constant volume and constant internal energy. Three modes of end-gas combustion were identified and discussed below: (1) normal flame propagation without autoignition, (2) autoignition without detonation development, and (3) detonation development.

As shown in Table 1, no end-gas autoignition occurs in case 1. Based on case 1 without end-gas autoignition, increase in temperature (case 2) or pressure (case 3) or chamber length (case 4) causes autoignition to happen but there is no detonation development. Based on case 2 with end-gas autoignition but no detonation, increase in temperature (case 5) or pressure (case 6) or chamber length (case 7) causes detonation development to happen. Therefore, the combustion mode of end-gas depends on at least three factors: initial temperature, initial pressure, and chamber size.

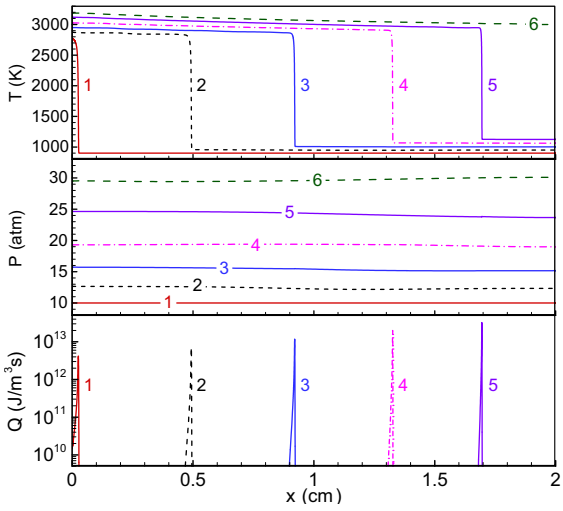

Fig. 2. Temporal evolution of temperature, pressure, and heat release rate distributions for case 1 with L = 2 cm, T_0 = 900 K and P_0 = 10 atm. The time sequence from line #1 to line #6 is: 1—0 μs, 2—120.36 μs, 3—240.97 μs, 4—361.44 μs, 5—481.85 μs, and 6—602.36 μs.

3.1. Normal flame propagation without autoignition

For case 1 with relative low initial temperature and pressure of T_0 = 900 K and P_0 = 10 atm, the ignition delay time of end-gas is relative long, which makes the Livengood–Wu integral [10] to be less than unity. Therefore, all the fresh mixture is consumed by the propagating flame front and end-gas autoignition does not happen. The temporal evolution of temperature, pressure, and heat release rate distributions for case 1 is plotted in Fig. 2 (the time sequence is described for different lines in the figure caption), which indicates normal flame propagation without end-gas autoignition. The pressure is shown to be nearly uniformly distributed, indicating that constant-pressure combustion occurs (which will also be demonstrated by the pressure-specific volume diagram in due course). The maximum heat release rate is shown to continuously increase. This is because that the temperature of unburned gas continuously increases due to compression. For example, in Fig. 2 the unburned gas temperature for line #5 at t = 481.85 μs is 1124 K, which is 224 K higher than that (900 K) for line #1 at t = 0 μs.

In simulation the flame/autoignition/reaction/detonation front, X_f, was defined as the position of local peak heat release rate. Therefore, the absolute propagation speed is $S = dX_f/dt$. The flame propagation speed for case 1 is shown in Fig. 3. It is observed that there is strong oscillation in flame propagation speed. This oscillation is caused by pressure wave-induced backward and forward flow in the closed chamber: negative flow speed reduces the flame propagation speed when the pressure wave propagates from the right to the left; and positive flow speed increases the flame propagation speed when the pressure wave is reflected on the left boundary and propagates to the right. Similar observation was found in experiments for

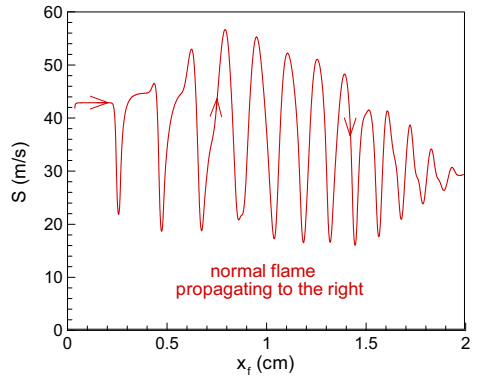

Fig. 3. Change of the flame propagation speed, $S = dx_f/dt$, with the flame front position, x_f (case 1).

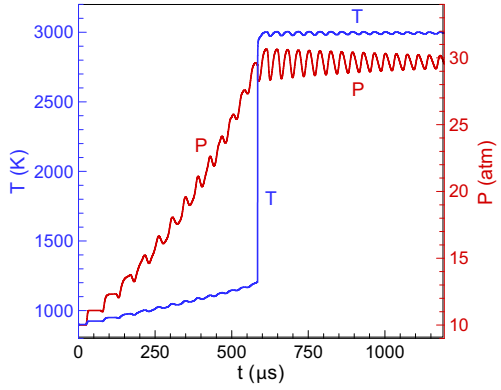

Fig. 4. Temporal evolution of temperature and pressure at the right boundary (case 1). For case 1, the equilibrium temperature and pressure are 3078 K and 30.0 atm, respectively.

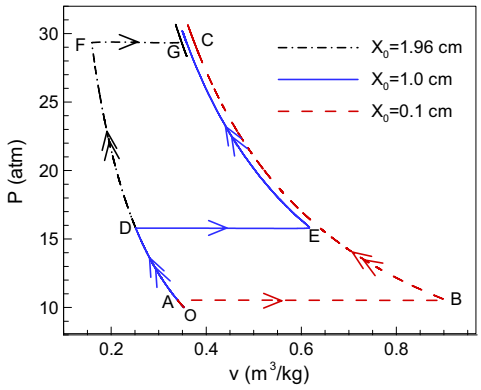

Fig. 5. The pressure versus specific volume, P-v, diagrams for particles at different initial positions of X_0 = 0.1, 1.0 and 1.96 cm (case 1 with the equilibrium pressure of 30.0 atm). Single arrow denotes constant-pressure combustion process (v increases); and double arrow denotes compression process (v decreases).

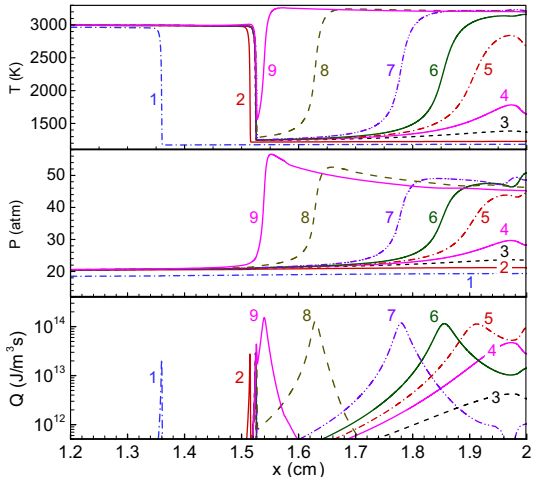

Fig. 6. Temporal evolution of temperature, pressure, and heat release rate distributions for case 2 with L = 2 cm, T_0 = 1000 K and P_0 = 10 atm. The time sequence from line #1 to line #9 is: 1—282.81 μs, 2—320.83 μs, 3—323.68 μs, 4—323.83 μs, 5—323.91 μs, 6—323.99 μs, 7—324.15 μs, 8—324.62 μs, and 9—325.02 μs.

hydrogen/air flame propagating in a closed duct [52]. For the displacement speed defined as S-u_f (where u_f is the local flow speed at the flame front) [53], there is no oscillation and it monotonically increases since the heat release rate continuously increases due to compression (see Fig. 2).

The temporal evolution of temperature and pressure at the right boundary is depicted in Fig. 4. Slight oscillation is observed and the amplitude of the pressure oscillation is within 2.5 atm. Such oscillation is also caused by the back-and-forth propagation of pressure wave in the closed chamber. After all the mixture is consumed by the propagating flame front (i.e., $t > 586$ μs), the temperature and pressure are shown to approach to their equilibrium values of $T_e = 3078$ K and $P_e = 30.0$ atm.

The thermal states of flow particles at different initial positions were tracked. The P-v (pressure versus specific volume) diagrams for three particles initially at X_0 = 0.1, 1.0 and 1.96 cm are shown in Fig. 5. Each particle goes through three stages: compression, combustion and compression. For example, for the flow particle initially at X_0 = 1.0 cm, it is first compressed along OAD in Fig. 5; then it goes through the flame front along DE; and finally it is compressed again along EG. When all the mixture is consumed (around points G and C in Fig. 5), compression and expansion occur due to the back-and-forth propagation of pressure wave. It is noticed that all the combustion processes (AB, DE and FG in Fig. 5) occur at nearly constant pressure. Therefore, constant-pressure rather than constant-volume combustion in fact occurs for flame propagation in a closed chamber without autoignition. This is also indicated by the nearly constant-pressure distribution at different times shown in Fig. 2.

3.2. Autoignition without detonation development

According to the Livengood–Wu integral [10], decrease in ignition delay time (by increasing the initial temperature or pressure) and increase in flame propagation time (by increasing the chamber length) both help to induce end-gas autoignition. Compared to case 1 without autoignition, cases 2–4 have larger initial temperature, pressure, and chamber length, respectively, and end-gas autoignition occurs in these three cases. As shown in the Supplementary Material, the Livengood–Wu integral can well predict the autoignition of hydrogen/air.

When the initial temperature is increased from T_0 = 900 K to T_0= 1000 K (from case 1 to case 2), the ignition delay time is greatly reduced and thereby end-gas autoignition occurs before all the mixture is consumed by the propagating flame front. The temperature, pressure, and heat release rate distributions for case 2 are plotted in Fig. 6. Since the pressure wave reflected on the right boundary further increases the local temperature and reactivity, end-gas autoignition starts near the right boundary (see line #3 for t = 323.68 μs in Fig. 6). For line #3, the temperature and pressure of end-gas are above 1200 K and 20 atm, respectively. The autoignition front is shown to propagate to the left and collide with the flame front propagating to the right at $x \approx 1.52$ cm (see line #9 in Fig. 6). It is noted that the time difference between lines #9 and #3 is 1.34 μs. Therefore,

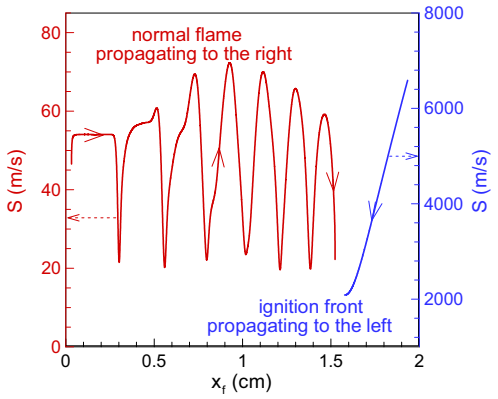

Fig. 7. Change of the propagation speed, $S = dx_f/dt$, with the position of flame or ignition front, x_f (case 2). It is note that S is negative for the ignition front since it propagates to the left.

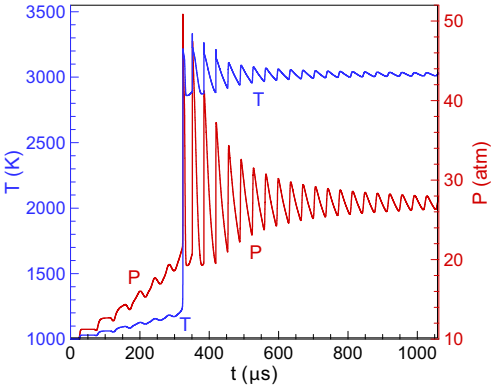

Fig. 8. Temporal evolution of temperature and pressure at the right boundary (case 2). For case 2, the equilibrium temperature and pressure are 3110 K and 27.3 atm, respectively.

the average propagation speed of the autoignition front is around 3500 m/s, which is much higher than the local sound speed and C-J detonation speed. Moreover, it is observed that the pressure rises to around 45 atm due to the rapid heat release from end-gas autoignition. The pressure can locally build up since the autoignition front propagates much faster than the pressure/acoustic wave. Due to the same reason, there is no coherent coupling between the autoignition front and pressure wave (The pressure wave does promote autoignition; while autoignition does not strength the pressure wave). Consequently, there is no detonation development and the maximum pressure is much less than that in a detonation.

The propagation speeds of flame front and autoignition front are shown in Fig. 7. Similar to case 1, strong oscillation is observed for the flame propagation speed and this oscillation is also caused by pressure wave-induced backward and forward flow in the closed chamber. The autoignition front is shown to propagate to the left at the speed of 2000 ~ 6000 m/s, which is two-order of magnitude larger than the flame propagation speed. As mentioned before, the speed of autoignition front is higher than the local sound speed and C-J detonation speed.

The temporal evolution of temperature and pressure at the right boundary is shown in Fig. 8. Strong pressure oscillation is observed after end-gas autoignition occurring at $t = 323.68$ μs. This pressure oscillation is similar to the conventional knock observed by Wang et al. [4]. The maximum amplitude of pressure oscillation is around 20 atm, which is one-order larger than 2.5 atm for case 1 without end-gas autoignition. Therefore, even without detonation

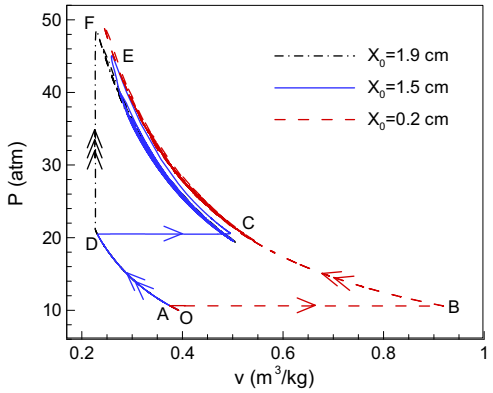

Fig. 9. P-v diagrams for particles at different initial positions of $X_0 = 0.2$, 1.5 and 1.9 cm (case 2 with the equilibrium pressure of 27.3 atm). Single arrow denotes constant-pressure combustion process (v increases); double arrow denotes compression process (v decreases); and triple arrow denotes nearly-constant-volume ignition process (v does not change).

development, end-gas autoignition can still induce strong pressure oscillation.

The P-v diagrams for particles at different initial positions are plotted in Fig. 9 for case 2. It is observed that particles initially at $X_0 = 0.2$ and 1.5 cm go through three stages: compression, constant-pressure combustion, and compression, which is similar to those shown in Fig. 5 for case 1. However, the particle initially at $X_0 = 1.9$ cm is first compressed along OAD in Fig. 9; then it goes through nearly constant-volume autoignition along DF; and finally expansion occurs. It is the nearly constant-volume autoignition that causes the rapid pressure rise observed in Fig. 6 and Fig. 8. Such pressure rise generates pressure wave (much stronger than case 1 without autoignition) propagating back-and-forth in the closed chamber. Consequently, as shown in Fig. 8, strong pressure oscillation occurs. Therefore, end-gas autoignition makes the combustion mode to switch from constant-pressure to constant-volume and it can generate strong pressure waves which induce engine knock.

Compared to case 1, case 2 has higher initial temperature and thereby end-gas autoignition happens. As mentioned in the beginning of this section, end-gas autoignition can also be induced by increasing the initial pressure (case 3) or chamber length (case 4). This is demonstrated by the results for case 3 and case 4 shown in Fig. 10(a) and (b), respectively. Similar to that in Fig. 8 for case 2, strong pressure oscillation is also observed for these two cases with end-gas autoignition.

3.3. Detonation development

In cases 2–4, only autoignition occurs and there is no detonation development. Wang et al. [54] found that detonation can lead to super-knock with destructively strong pressure oscillation and thereby it must be avoided in engines. Detonation occurs when the reactivity of unburned end-gas is further enhanced by increasing the initial temperature (case 5) or initial pressure (case 6). Besides, detonation is found to be developed from an autoignition front when the chamber length is large enough (case 7). It is noted that the detonation is not like the normal one. This is because in our simulations of cases 5–7, the detonation is developed and it propagates towards an auto-igniting mixture (the mixture already has very high reactivity and chemical reaction can take place before the shock wave). Moreover, the sonic condition at the end of heat release was not reached.

When the initial temperature is increased from $T_0 = 1000$ K to $T_0 = 1100$ K (from case 2 to case 5), detonation development occurs as shown in Fig. 11. At the beginning, the normal flame propagates to the right (e.g., line #1 in Fig. 11). At $t \approx 80$ μs, detonation starts

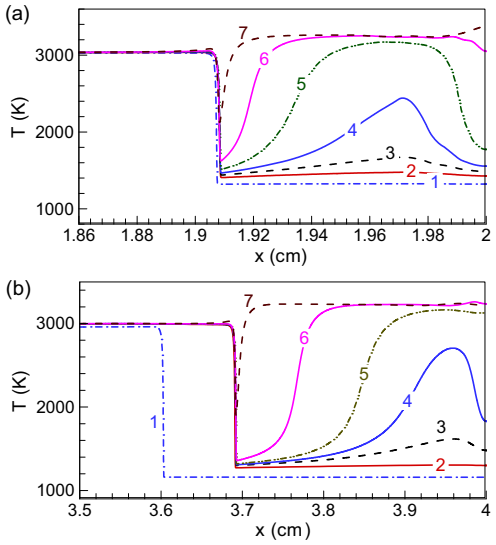

Fig. 10. Temporal evolution of temperature distribution for (a) case 3 with L = 2 cm, T_0 = 900 K and P_0 = 20 atm (the time sequence from line #1 to line #7 is: 1—687.26 μs, 2—688.01 μs, 3—688.09 μs, 4—688.13 μs, 5—688.16 μs, 6—688.20 μs, and 7—688.24 μs); (b), case 4 with L = 4 cm, T_0 = 900 K and P_0 = 10 atm (the time sequence from line #1 to line #7 is: 1—1034.59 μs, 2—1061.64 μs, 3—1062.10 μs, 4—1062.18 μs, 5—1062.26 μs, 6—1062.41 μs, and 7—1062.65 μs).

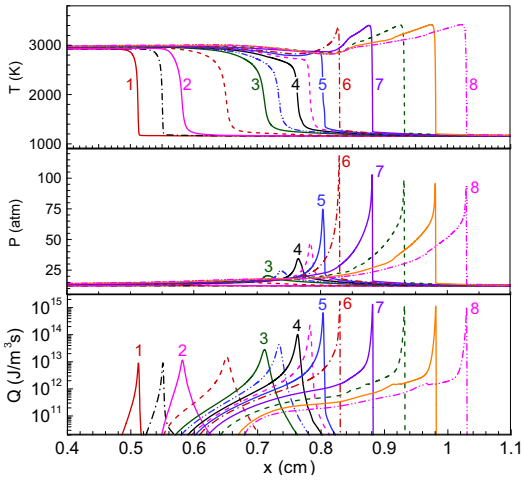

Fig. 11. Temporal evolution of temperature, pressure, and heat release rate distributions for case 5 with L = 2.0 cm, T_0 = 1100 K and P_0 = 10 atm. The time sequence from line #1 to line #8 is: 1—75.00 μs, 2—83.01 μs, 3—86.00 μs, 4—86.50 μs, 5—86.76 μs, 6—86.88 μs, 7—87.11 μs, and 8—87.81 μs.

to develop and there is rapid increase in both peak pressure and peak heat release rate (from line #2 to line #6 in Fig. 11). The peak pressure reaches 130 atm, which is about five times of the equilibrium value of P_e = 25.2 atm (as listed in Table 1 for case 5). At $t \approx 87\mu s$, the detonation is fully developed and afterwards the end-gas is consumed by the self-sustaining detonation propagating to the right (lines #6-#8 in Fig. 11).

The propagation speed of the reaction front for case 5 is shown in Fig. 12. The initial normal flame propagates to the right at the speed of 70 m/s (point A in Fig. 12). At point B, the propagation speed is reduced to 35 m/s. This is because that the left-propagating pressure wave induces backward flow in the closed chamber. Therefore, flame propagation speed oscillation similar to those shown in Fig. 3 and Fig. 7 (respectively for case 1 and case 2) would appear for case 5 if there is no detonation development. It is observed that there is rapid increase of propagation speed from 80 m/s (point #1) to 2233 m/s

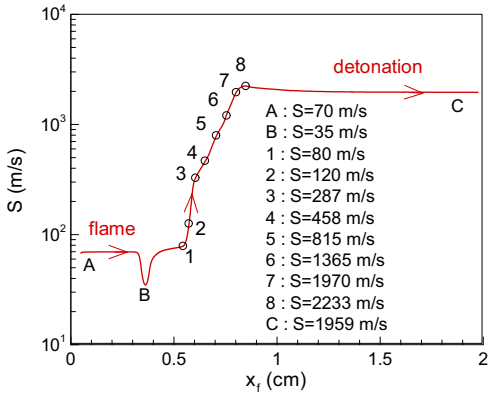

Fig. 12. Change of the propagation speed, $S = dx_f/dt$, with the position of flame/ignition/detonation front, x_f (case 5). The C-J detonation speed is around 1960 m/s. It is noted that points 1–8 in this figure correspond to lines 1–8 in Fig. 14, not those in Fig. 11.

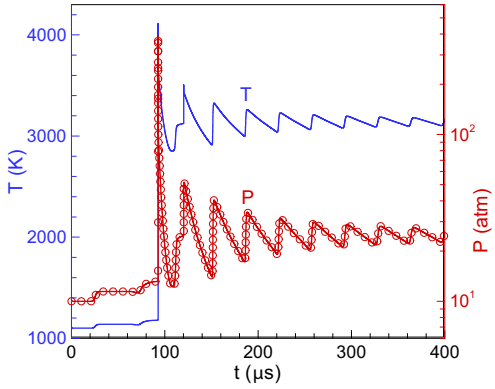

Fig. 13. Temporal evolution of temperature and pressure at the right boundary (case 5). For case 5, the equilibrium temperature and pressure are 3140 K and 25.2 atm, respectively.

(point #8), which corresponds to the detonation development process to be explained later in Fig. 14. After the detonation development, self-sustaining detonation propagates to the right approaching to the C-J detonation speed of 1960 m/s (point C in Fig. 12).

The temporal evolution of temperature and pressure at the right boundary is shown in Fig. 13. Extremely high pressure around 300 atm is observed when the detonation reflects at the right boundary. The peak pressure is about six times of that for case 2 with end-gas autoignition but no detonation (see Fig. 8). Therefore, detonation development can cause extremely large amplitude of pressure oscillation, which is close to the super-knock observed by Wang et al. [4, 54].

To explain the deflagration to detonation transition process shown in Fig. 11, we plotted the enlarged display of temperature and pressure distributions during detonation development in Fig. 14. As mentioned before, the reaction front propagation speeds at times corresponding to lines #1–8 in Fig. 14 are marked by points #1–8 in Fig. 12. At t = 80 μs (line #1 in Fig. 14), the pressure is nearly uniformly distributed in the whole domain while there is obvious temperature gradient in the range of $0.554 \le x \le 0.6$ cm (between points A and B in Fig. 14b), which is in the upstream of the preheat zone. Such temperature gradient is caused by heat release from local autoignition and it can induce detonation development according to the theory of Zel'dovich [8, 11] on detonation generated by reactivity gradient (more details can also be found in Ref. [13]). The end-gas in the range of $0.554 \le x \le 0.6$ cm at t = 80 μs has very high reactivity and is close to autoignition. Due to the negative temperature gradient in $0.554 \le x \le 0.6$ cm, autoignition first occurs around x = 0.554 cm

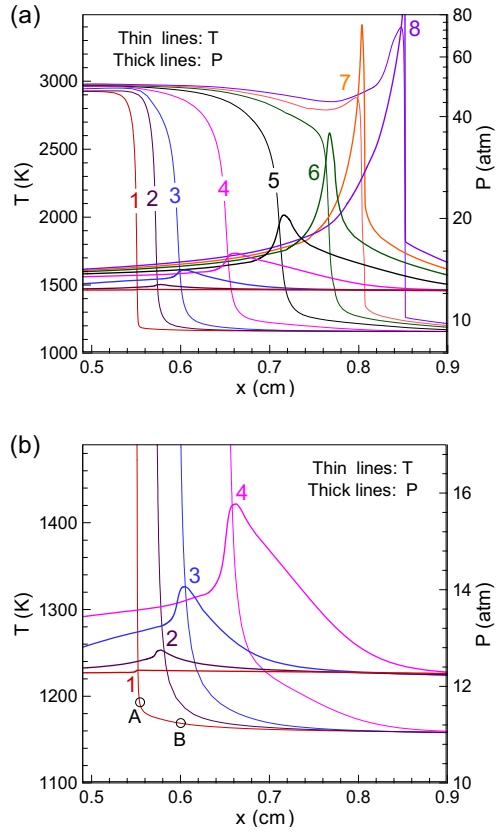

Fig. 14. Enlarged display of temperature and pressure distributions during detonation development in case 5. The time sequence from line #1 to line #8 is: 1—80.00 μs, 2—82.50 μs, 3—83.55 μs, 4—85.00 μs, 5—86.00 μs, 6—86.52 μs, 7—86.76 μs, and 8—86.97 μs.

(point A in Fig. 14b) and the local heat release generates pressure pulse/wave propagating to the right, where the H_2/air premixture is on the threshold of autoignition. The pressure wave initiates autoignition of this premixture, the heat release of which further strengthens the pressure wave. Therefore, the autoignition front accelerates and interacts coherently with the pressure wave. Such coherent coupling between pressure wave and local autoignition (or chemical reaction) results in local pressure build-up (line #2 in Fig. 14) and acceleration of the autoignition front propagation [7]. At the beginning (line #2 in Fig. 14), the pressure wave propagates much faster than the reaction/autoignition front (according to point #2 in Fig. 12, the speed of the reaction front is only 120 m/s). Then, the unburned end-gas immediately behind the pressure wave has higher reactivity after being compressed, which results in abrupt acceleration in the propagation speed (lines #2–7 Fig. 14 and points #2–7 in Fig. 12). Eventually, the enhanced coherent interaction between pressure wave and local chemical reaction leads to the formation of an over-driven detonation wave (line #8 in Fig. 14), which slows down to become a self-sustaining detonation propagating to the right (lines #7-8 in Fig. 11).

To give more details on the detonation development process, in Fig. 15 we plotted the *P*-*v* and *P*-λ diagrams for particles at different initial positions. The reaction process, λ, was defined as the percentage of hydrogen consumed, i.e., $\lambda = 1 - Y_{H_2}/Y^0_{H_2}$ (where Y_{H_2} is the mass fraction of hydrogen and the superscript 0 indicates the state in the initial unburned end-gas). Particle #1 initially at $X_0 = 0.52$ cm is first compressed along OA in Fig. 15(a); then it goes through constant-pressure combustion along AK before autoignition happens; and finally it is compressed along KJ. This behavior is similar to that of the particle initially at $X_0 = 1.0$ cm in case 2 shown in Fig. 9. Particle #2 at $X_0 = 0.57$ cm is located at the position where detonation development starts (see Fig. 14). Both pressure and specific volume are shown to slightly increase when particle #2 goes through the combustion process along AJ in Fig. 15(a). The pressure rise is due to heat release from chemical reaction while the increase of specific volume is due to expansion (which also reduces pressure rise) after being passed by the pressure wave. Particles #3–5 experience the transition to detonation; while particle #6 goes through the over-driven detonation after the transition process. For particle #6, it is first compressed by the propagating flame along OA; then it goes through a shock wave along ABCDEF; and finally it experiences expansion along FG. Similar processes also happen to particle #7 which goes through a self-sustaining detonation propagating close to the C-J speed. It is noticed in Fig. 15(b) that, for particles #4–7 the reaction progress is not close to zero when the peak pressure is reached, indicating that chemical reaction already takes place within and before the shock wave. This is because particles #4–7 have very high reactivity and are on the threshold of autoignition before it goes through the shock wave. Therefore, curves AC, AD, AE and AF are not Hugoniot curves; and the results in Fig. 15 are not similar to those for traditional ZND detonation structure, in which chemical reaction occurs only after the peak pressure (the von Neumann spike) is reached.

Compared to case 2 without detonation development, case 5 has higher initial temperature and thereby detonation occurs. Detonation development can also be triggered by increasing the initial pressure. In case 6, the initial pressure is increased from 10 atm (case 2) to 40 atm (case 6) while the initial temperature of $T_0 = 1000$ K and the chamber length of $L = 2$ cm are both kept unchanged. The results for case 6 in Fig. 16 show the detonation development and propagation

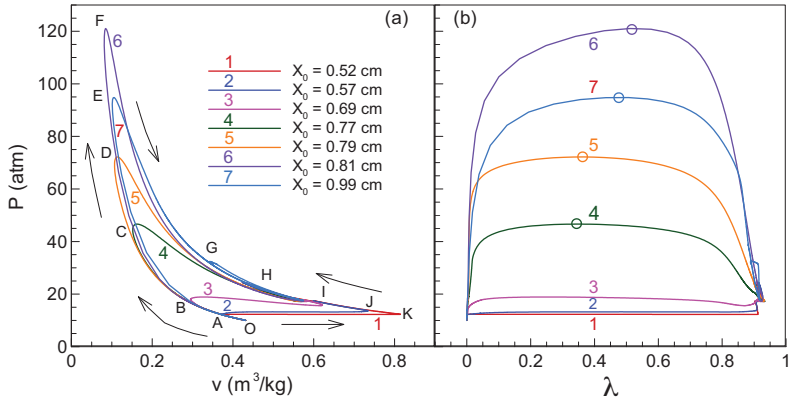

Fig. 15. (a) P-v and (b) P-λ diagrams for particles at different initial positions of $X_0 = 0.52$, 0.57, 0.69, 0.77, 0.79, 0.81, and 0.99 cm (case 5). The open circles in the right figure denote the maximum pressure.

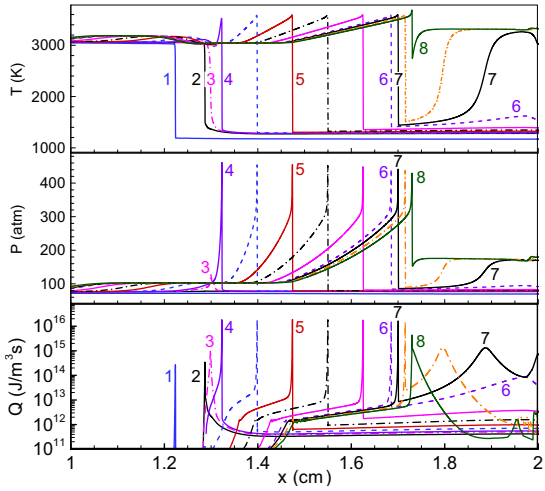

Fig. 16. Temporal evolution of temperature, pressure, and heat release rate distributions for case 6 with L = 2.0 cm, T_0 = 1000 K and P_0 = 40 atm. The time sequence from line #1 to line #8 is: 1—374.71 μs, 2—398.35 μs, 3—398.74 μs, 4—398.89 μs, 5—399.67 μs, 6—400.74 μs, 7—400.82 μs, and 8—400.98 μs.

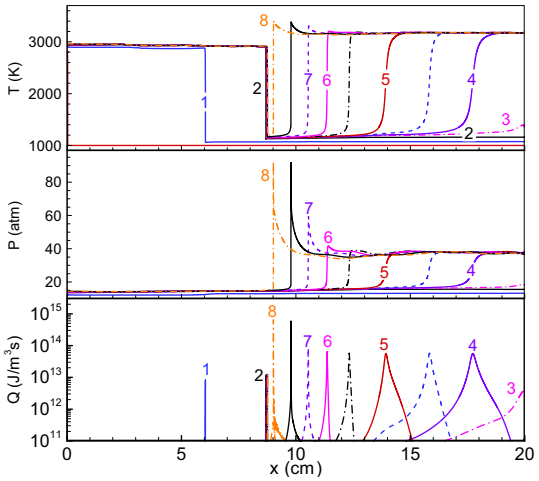

Fig. 17. Temporal evolution of temperature, pressure, and heat release rate distributions for case 7 with L = 20.0 cm, T_0 = 1000 K and P_0 = 10 atm. The time sequence from line #1 to line #8 is: 1—975.59 μs, 2—1484.38 μs, 3—1494.14 μs, 4—1495.12 μs, 5—1497.07 μs, 6—1502.93 μs, 7—1506.84 μs, and 8—1514.65 μs.

processes. In Fig. 16: line #1 corresponds to normal flame propagating to the right; lines #2–4 correspond to the detonation development process; and lines #4-6 correspond to self-sustaining detonation propagating to the right. Unlike the results shown in Fig. 11 for case 5, Fig. 16 indicates that end-gas autoignition happens during the detonation propagation process (lines #6–8 in Fig. 16). The end-gas in the range of $1.73 \le x \le 2.0$ cm is consumed by the autoignition front rather than the detonation wave. At $t = 400.98$ μs (line #8 in Fig. 16), the autoignition front propagating to the left collides with the detonation propagating to the right at $x \approx 1.73$ cm. All the premixture is burned after the collision and then the detonation becomes a shock wave propagating to the right, which will be reflected at the right boundary. From line #6 to line #8 in Fig. 16, the averaged propagation speed of the detonation is around 1800 m/s while that of the autoignition front is about 9600 m/s. Therefore, the autoignition front propagates much faster than the detonation wave.

Compared to case 2 (in which there is end-gas autoignition but no detonation development, as shown in Fig. 6), case 7 has the same initial temperature and pressure ($T_0 = 1000$ K and $P_0 = 10$ atm) but much larger chamber size of $L = 20$ cm. The results for case 7 are shown in Fig. 17, which demonstrates that detonation development does occur when only the chamber size is enlarged. In Fig. 17, line #1 corresponds to normal flame propagating to the right. End-gas autoignition starts at the right boundary around $t = 1494.14$ μs (line #3 in Fig. 17) and the autoignition front is shown to propagate to the left (lines #3–#5). This is similar to what happens in case 2 as shown in Fig. 6. However, the distance travelled by the autoignition front in case 7 with $L = 20$ cm is above 5 cm (see Fig. 17); while that in case 2 with $L = 2$ cm is less than 0.5 cm as (see Fig. 6). Consequently, in the smaller chamber with $L = 2$ cm, all the end-gas is quickly consumed by the autoignition front (see lines #5-9 in Fig. 6); while in the larger chamber with $L = 20$ cm, there is enough time for detonation development from the propagating autoignition front (see lines #6–8 in Fig. 17). We also conduct simulations for the case of $L = 10$ cm, $T_0 = 1000$ K and $P_0 = 10$ atm, in which detonation development is not observed (i.e., similar to case 2 shown in Fig. 6). Therefore, the close chamber should be long enough so that detonation can be developed from the propagating autoignition front.

In a brief summary, the main condition for detonation development is that the end-gas should be reactive enough so that it is on the threshold of autoignition. The pressure pulse/wave generated by local heat release passes through unburned mixture and initiates the chemical reaction and heat release there since the temperature and pressure of this unburned mixture both increase after being compressed by the pressure wave. The heat release further strengthens the pressure wave, which also induce further chemical reaction and heat release. Therefore, a coherent coupling between pressure wave and chemical reaction is a reached and it eventually leads to autoignition front acceleration and detonation development.

It is noted that here we only considered stoichiometric mixture. With the decrease of the equivalence ratio, the duration of heat release becomes longer and thereby the coherent coupling between pressure wave and heat release becomes weaker. Consequently, it is more difficult for detonation development to happen in a leaner mixture.

3.4. Influence of ignition process on end-gas autoignition and detonation development

In the previous three sub-sections, we found that high reactivity of end-gas (achieved by increasing the initial temperature or pressure) promotes autoignition and detonation development. To further demonstrate the validity of this observation, we considered the end-gas initially at different values of ignition progress. The ignition progress was defined as $c = t_0/\tau_0$, where τ_0 is the constant-volume homogeneous ignition delay time and t_0 is the time at which the states (temperature, pressure, and mass fraction of all species) in the constant-volume homogeneous ignition progress are specified as the initial states for end-gas in 1D simulation. Therefore, when $c = 0$, the end-gas contains only hydrogen and air and all the results in the previous three sub-sections are obtained for $c = 0$. With the increase of the value of ignition progress, c, the end-gas is more prone to ignite and thereby has higher reactivity. Similar method was used in the study of Martz et al. [35] though they used a different definition of ignition progress based on temperature rise.

In case 1 (see Fig. 2), there is no end-gas autoignition and detonation development when the ignition process is zero (i.e., $c = 0$). With the increase of the ignition process, Fig. 18 shows that end-gas autoignition and detonation development both appear. Similarly, for case with end-gas autoignition and without detonation development at $c = 0$ (see Fig. 6), Fig. 19 shows that detonation development can happen when the value of ignition progress reaches 80%. Moreover, comparison between Fig. 19 and Fig. 6 indicates that end-gas autoignition occurs earlier at larger value of ignition progress, c. Therefore, the results in Fig. 18 and Fig. 19 further demonstrates

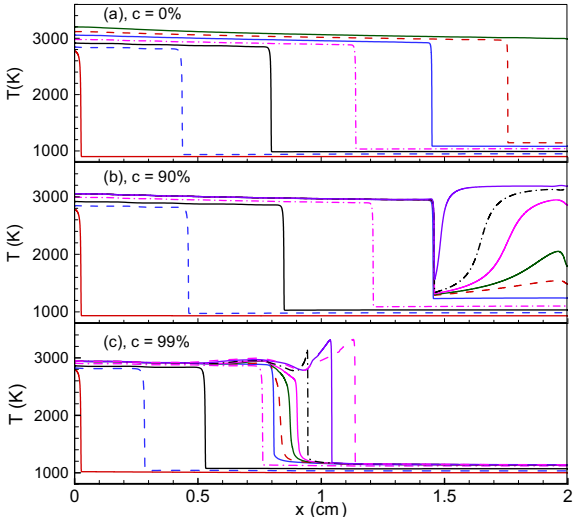

Fig. 18. Temporal evolution of temperature distributions at different values of ignition process (c = 0%, 90% and 99%) for case 1 with L = 2 cm, T_0 = 900 K and P_0 = 10 atm.

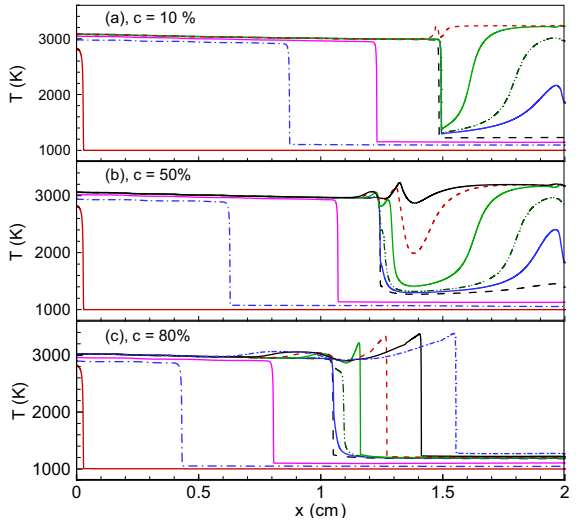

Fig. 19. Temporal evolution of temperature distributions at different values of ignition process (c = 10%, 50% and 80%) for case 2 with L = 2 cm, T_0 = 1000 K and P_0 = 10 atm.

that high reactivity of end-gas promotes autoignition and detonation development.

4. Conclusions

Combustion of end-gas in a closed chamber filled with stoichiometric H_2/air mixture was studied by 1D simulation considering detailed chemistry. Depending on the chamber size as well as the initial temperature and pressure, three modes of end-gas combustion were identified: (1) normal flame propagation without autoignition, (2) autoignition without detonation development, and (3) detonation development.

When there is no end-gas autoignition, the amplitude of pressure oscillation is small and the peak pressure is close to the equilibrium value under the conditions of constant volume and constant internal energy. Each flow particle was found to go through three stages: compression, combustion and compression. It was demonstrated that constant-pressure rather than constant-volume combustion happens to flame propagation in a closed chamber without autoignition.

When there is end-gas autoignition but no detonation development, high amplitude of pressure oscillation similar to conventional knock was observed. It is end-gas autoignition that makes the combustion mode to switch from constant-pressure to constant-volume and generates strong pressure waves which induce engine knock. The autoignition front was found to propagate much faster than the pressure/acoustic wave and thereby there is no coherent coupling between the pressure wave and chemical reaction.

When there is detonation development, extremely high amplitude of pressure oscillation was observed, which is similar to superknock observed by Wang et al. [4, 54]. Negative temperature gradient was found to appear in the upstream of the preheat zone due to the heat release from local autoignition (between points A and B in Fig. 14b) and it triggers detonation development according to the reactivity gradient theory of Zel'dovich [8, 11]. Detailed analysis indicated that coherent coupling between pressure wave and chemical reaction leads to autoignition front acceleration and detonation development. Besides, it was found that the detonation development can be promoted by increasing the initial temperature, pressure, or chamber size.

Furthermore, simulations on end-gas at different ignition progress were conducted. It was demonstrated that the reactivity of end-gas determines whether end-gas autoignition and detonation development occur. At higher initial temperature and pressure, end-gas is more reactive and thereby end-gas autoignition and detonation development are more prone to occur.

It is noted that 1D simulation was conducted here and the initial temperature of end-gas was uniformly distributed. Therefore, the effects of temperature inhomogeneity (local hot-spot) and turbulent transport on the end-gas combustion were not examined, which certainly deserve further investigation.

It is also noted that in multi-dimensional flows, deflagration-to-detonation transition usually occurs with the help of the appearance of obstacles, boundary layers, or turbulent mixing (see the review paper of Oran and Gamezo [55]). In 1D or quasi 1D flows, in previous studies detonation was found to be developed only when there is temperature/concentration gradient initially specified (e.g., [13]) or when there is friction-induced preheating [56–58]. However, the present simulation demonstrated for the first time that even in 1D flow only with an initial propagating flame, detonation can still be developed when the reactivity of end-gas is high enough.

Acknowledgments

This work was supported by National Natural Science Foundation of China (Nos. 51322602 and 51136005) and State Key Laboratory of Engines at Tianjin University (No. K2014-01). We acknowledge the helpful discussions with Professor Yiguang Ju at Princeton University and Professor Zhi Wang at Tsinghua University. We also thank the reviewers for providing helpful comments and suggestions.

Supplementary materials

Supplementary material associated with this article can be found, in the online version, at doi:10.1016/j.combustflame.2015.08.018.

References

[1] P.K. Senachin, V.S. Babkin, Combust. Explo. Shock Waves 18 (1982) 1–5.
[2] Z. Wang, X. He, J. Wang, S. Shuai, F. Xu, D. Yang, Energ. Convers. Manage. 51 (2010) 908–917.
[3] G.T. Kalghatgi, D. Bradley, Int J. Engine Res 13 (2012) 399–414.
[4] Z. Wang, H. Liu, T. Song, Y. Qi, X. He, S. Shuai, J. Wang, Int J. Engine Res. 16 (2015) 166–180.
[5] J.B. Heywood, Internal Combustion Engines Fundamentals, McGraw Hill, New York, 1988.
[6] D. Bradley, G.T. Kalghatgi, M. Golombok, J. Yeo, Proc. Combust. Inst. 26 (1996) 2653–2660.
[7] J. Pan, G. Shu, H. Wei, Combust. Sci. Technol. 186 (2014) 192–209.
[8] Y. Zeldovich, Combust. Flame 39 (1980) 211–214.
[9] J.H.S. Lee, The Detonation Phenomenon, Cambridge University Press, Cambridge, 2008.

[10] J.C. Livengood, P.C. Wu, Proc. Combust. Inst. 5 (1955) 347–356.
[11] Y.B. Zeldovich, V.B. Librovich, G.M. Makhviladze, G.I. Sivashinsky, Acta Astronaut 15 (1970) 313–321.
[12] D. Bradley, C. Morley, X.J. Gu, D.R. Emerson, SAE-2002-01-2868, 2002.
[13] X.J. Gu, D.R. Emerson, D. Bradley, Combust. Flame 133 (2003) 63–74.
[14] D. Bradley, G.T. Kalghatgi, Combust. Flame 156 (2009) 2307–2318.
[15] D. Bradley, Philos. T. Roy. Soc. A. 370 (2012) 689–714.
[16] L.S. Kagan, P.V. Gordon, G.I. Sivashinsky, Combust. Theor. Model. 16 (2012) 1–12.
[17] L. Kagan, G. Sivashinsky, Proc. Combust. Inst. 34 (2013) 857–863.
[18] N. Kawahara, E. Tomita, Y. Sakata, Proc. Combust. Inst. 31 (2007) 2999–3006.
[19] N. Kawahara, E. Tomita, Int. J. Hydrogen Energy 34 (2009) 3156–3163.
[20] J.F. Griffiths, J.P. MacNamara, C.G.W. Sheppard, D.A. Turton, B.J. Whitaker, Fuel 17 (2002) 2219–2225.
[21] M. Pöschl, T. Sattelmayer, Combust. Flame 153 (2008) 562–573.
[22] Y. Nagano, T. Ohira, M. Oomaka, Y. Uyama, T. Kitagawa, One-dimensional Flame Propagation and Auto-ignition of End Gas in Constant Volume Vessel, in: The Eighth International Conference on Modeling and Diagnostics for Advanced Engine Systems (COMODIA 2012), Fukuoka, Japan, 2012.
[23] Y. Qi, X. He, Z. Wang, J. Wang, H. Zhang, Y. Jiang, Int. J. Hydrogen Energy 40 (2015) 2377–2385.
[24] J. Pan, C.G.W. Sheppard, SAE-942060, 1994.
[25] J. Pan, C.G.W. Sheppard, A. Tindall, SAE-982616, 1998.
[26] M.A. Liberman, M.F. Ivanov, O.E. Peil, D.M. Valiev, L.E. Eriksson, Combust. Sci. Technol. 177 (2004) 151–182.
[27] M.A. Liberman, M.F. Ivanov, D.M. Valiev, L.E. Eriksson, Combust. Sci. Technol. 178 (2006) 1613–1647.
[28] Z. Wang, Y. Wang, R.D. Reitz, Energ. Fuel. 26 (2012) 7107–7119.
[29] H. Wei, Y. Shang, C. Chen, D. Gao, D. Feng, Int. J. Hydrogen Energy 39 (2014) 21265–21274.
[30] J.H. Chen, E.R. Hawkes, R. Sankaran, S.D. Mason, H.G. Im, Combust. Flame 145 (2006) 128–144.
[31] C.S. Yoo, T. Lu, J.H. Chen, C.K. Law, Combust. Flame 158 (2011) 1727–1741.
[32] M.B. Luong, Z. Luo, T. Lu, S.H. Chung, C.S. Yoo, Combust. Flame 160 (2013) 2038–2047.
[33] M.B. Luong, T. Lu, S.H. Chung, C.S. Yoo, Combust. Flame 161 (2014) 2878–2889.
[34] Y. Ju, W. Sun, M.P. Burke, X. Gou, Z. Chen, Proc. Combust. Inst. 33 (2011) 1245–1251.
[35] J.B. Martz, H. Kwak, H.G. Im, G.A. Lavoie, D.N. Assanis, Proc. Combust. Inst. 33 (2011) 3001–3006.
[36] J.B. Martz, G.A. Lavoie, H.G. Im, R.J. Middleton, A. Babajimopoulos, D.N. Assanis, Combust. Flame 159 (2012) 2077–2086.
[37] H. Zhang, E.R. Hawkes, J.H. Chen, S. Kook, Proc. Combust. Inst. 34 (2013) 803–812.
[38] P. Dai, Z. Chen, S. Chen, Y. Ju, Proc. Combust. Inst. (2014) 35.
[39] H. Terashima, M. Koshi, Combust. Flame 162 (2015) 1944–1956.
[40] R.J. Kee, J.F. Grcar, M.D. Smooke, J.A. Miller, Sandia National Laboratories-SAND85-8240, 1985.
[41] Z. Chen, Combust. Flame 157 (2010) 2267–2276.
[42] Z. Chen, M.P. Burke, Y. Ju, Proc. Combust. Inst. 32 (2009) 1253–1260.
[43] G. Strang, SIAM J. Numer. Anal. 5 (1968) 506–517.
[44] P.N. Brown, G.D. Byrne, A.C. Hindmarsh, SIAM J. Sci. Comput 10 (1989) 1038–1051.
[45] J. Li, Z. Zhao, A. Kazakov, F.L. Dryer, Int. J. Chem. Kinet. 36 (2004) 566–575.
[46] R.J. Kee, F.M. Rupley, J.A. Miller, Sandia National Laboratories-SAND89-8009B, 1989.
[47] Z. Chen, M.P. Burke, Y. Ju, Proc. Combust. Inst 33 (2011) 1219–1226.
[48] Z. Chen, Combust. Flame 158 (2011) 291–300.
[49] H. Yu, W. Han, J. Santner, X. Gou, C.H. Sohn, Y. Ju, Z. Chen, Combust. Flame 161 (2014) 2815–2824.
[50] Z. Chen, Combust. Flame 162 (2015) 2242–2253.
[51] R. Zhou, J. Wang, Combust. Flame 159 (2012) 3632–3645.
[52] H. Xiao, X. Shen, J. Sun, Int. J. Hydrogen Energy 37 (2012) 11466–11473.
[53] D. Veynante, T. Poinsot, Theoretical and Numerical Combustion, Edwards, Philadelphia, 2005.
[54] Z. Wang, Y. Qi, X. He, J. Wang, S. Shuai, C.K. Law, Fuel 144 (2015) 222–227.
[55] E.S. Oran, V.N. Gamezo, Combust. Flame 148 (2007) 4–47.
[56] L. Kagan, G. Sivashinsky, Combust. Flame 154 (2008) 186–190.
[57] M.H. Wu, P. Burke, S.F. Son, R.A. Yetter, Proc. Combust. Inst. 31 (2007) 2429–2436.
[58] M.H. Wu, C.Y. Wang, Proc. Combust. Inst. 33 (2011) 2287–2293.
[59] R.F. Strickland-Constable, Symp. (Int.) Combust, in: 3Third Symposium on Combustion and Flame and Explosion Phenomena, 1949, pp. 229–235.